Direct observation and stochastic analysis on thermally activated nucleation and growth of individual magnetic domain

Fangfei Luo,[1] Kentaro Toyoki,[1,2,3] Chiharu Mitsumata,[4] Jiaqi Shen,[1] Ryoichi Nakatani,[1,2,3] and Yu Shiratsuchi[1,2,3,*]

1 Graduate School of Engineering, Osaka University, Suita, Osaka 565-0871, Japan

2 Division of Spintronics Research Network, Institute for Open and Transdisciplinary Research Initiatives, Osaka University, Suita, Osaka, 565-0871, Japan

3 Center for Spintronics Research Network, Osaka University, Toyonaka 560-8531, Japan

4 Faculty of Industrial Science and Technology, Tokyo University of Science, Katsushika, Tokyo 125-8585, Japan.

Abstract

The nucleation and subsequent growth of the reversed magnetic domain at a finite temperature are stochastic processes, which are analyzed using an ensemble of magnetic elements. In this study, we investigate the stochastics of magnetization reversal in multiple trials for the sole magnetic domain. Specifically, we utilize the robust magnetic domain structure formed in a dual-exchange-biased Pt/Co/Au/Cr_2O_3/Pt thin film. Our investigation encompasses the latency of reversed domain nucleation and the subsequent domain wall motion based on time-lapse magnetic domain observations. The time evolution of the magnetic domain is observed after applying a pulsed magnetic field superimposed on a DC field. Magnetization reversal is triggered by the nucleation of a small embryo with finite latency, followed by domain wall propagation. The nucleation probability of the embryo increases exponentially with the DC field, thus indicating that the nucleation process obeys the Poisson process. An analysis of the relaxation time for nucleation provides a suitable expression for the energy barrier. The nucleated domain wall propagates with temporal stops, thus indicating creep motion. The temperature dependence of the relaxation time and domain wall creep motion reveal that the magnetic anisotropy in the antiferromagnetic layer significantly affect both the energy barrier for nucleation and the depinning potential of domain wall propagation. This study provides comprehensive understanding into the coercivity mechanism and contributes to the thermal stability of magnetic/spintronic devices.

* Corresponding author: shiratsuchi@mat.eng.osaka-u. ac.jp.

1. Introduction

Controlling the magnetization direction in nanosized magnets such as thin magnetic layers and magnetic nanoparticles is a fundamental issue in magnetic materials. This pursuit encompasses the elucidation of the magnetization reversal process via a magnetic field cycle [1] and/or an electric current [2] as well as the stability of the magnetization direction against perturbation by a weak field, time, and temperature [3-6]. The hysteresis curve of magnetization as a function of the magnetic field is one of the most fundamental methods to characterize magnetic properties. In the case of ferromagnetic (FM) materials, coercivity, which is the magnetic field at which the magnetization becomes zero, is one of key performance parameter. Despite long history of research on magnetic materials, there is still unresolved problems on the coercivity mechanism, such as the Brown paradox [7]. The switching process relevant to coercivity is typically involved in the nucleation and growth of reversed magnetic domains, except in specific cases, such as coherent rotation. From an engineering perspective, nucleation and subsequent domain wall (DW) motion determine the thermal stability, switching energy, and switching speed of magnetic storage and spintronic devices. Therefore, the nucleation and growth of reversed magnetic domains must be elucidated.

Because the nucleation of the reversed magnetic domain and DW motion are time-dependent phenomena at a finite temperature involving the stochastic motion of the magnetic domain [4,8-13]. Hence, various approaches such as temperature [10], field-sweep-rate dependence of coercivity [8,11], time dependence of magnetization at a constant field [4,8,9,12,13], and time-lapse magnetic domain observation [4,8] were considered. In most previous studies, an ensemble of magnetic elements/magnetic domains was analyzed. Although the investigation for the individual and identical magnetic domain is a direct route to address the stochastics of magnetic domain motion, it has been lacking. This is partly due to the magnetic domain pattern during trial-by-trial reversal changes [4,14]. Previous studies attempted to extract the signal of an individual magnetic domain from the total signal [6,15]. In these studies, because the signal was obtained by sweeping the magnetic field, the individual stochastics of nucleation and subsequent DW propagation could not be distinguished easily. In this study, we address this issue using a robust magnetic domain structure formed in a dual exchange-biased system [16, 17]. Previously, we reported that the magnetic domain pattern in an exchange-biased Pt/Co/Au/Cr_2O_3/Pt thin film formed by zero-field cooling (ZFC) was robust against the magnetic field cycle [16]. Additionally, we reported that the magnetic

domain pattern can be recovered by removing the magnetic field with finite latency. The robustness of the magnetic domain pattern relies on a high exchange bias greater than the coercivity [18] and the absence of the training effect [19,20]. The induced exchange bias is oriented in the direction perpendicular to the film, i.e., the perpendicular exchange bias (PEB) is associated with the perpendicular magnetic anisotropy (PMA), which is suitable for both fundamental research and applications. Details regarding the PEB using Cr_2O_3 thin films are available in a previous review [21]. Furthermore, the PEB using Cr_2O_3 is versatile, as identified by their switching ability due to the magnetoelectric effect of Cr_2O_3 [22,23], which involves the electric field control of the stochastic motion of the magnetic domain. In this study, we exploit the robustness of the remnant magnetic domain pattern and investigate the time evolution of the magnetic domain during the recovery process. Our approach is based on multiple observations of the sole magnetic domain, which allows us to directly address the stochastics of the nucleation and subsequent growth of the reversed magnetic domain.

2. Experimental procedures and conditions

A Pt(2 nm)/Co(0.6 nm)/Au(1.0 nm)/Cr_2O_3(130 nm)/Pt(20 nm) thin film grown on α-Al_2O_3(0001) substrate was used as the sample. This stacking structure is similar to that of the previous film, which shows the abovementioned robust magnetic domain structure owing to the exchange bias [18]. The films were fabricated using a DC magnetron sputtering system. The details of the sample preparation are available in our previous study [18]. Structural characterization was performed via *in-situ* reflection high-energy electron diffraction (RHEED) and X-ray diffraction (XRD). The RHEED observations were performed using an electron beam accelerated at 25 kV. The XRD measurements were performed using Cu K_α irradiation. The accelerating voltage and emission current were 45 kV and 200 mA, respectively.

The magnetic properties were investigated based on magnetization curve measurements using a vibrating sample magnetometer (VSM), superconducting quantum interference device (SQUID) magnetometer, and magneto-optic Kerr effect (MOKE) magnetometry. A VSM was used to measure the magnetization curve at room temperature for applied field directions parallel and perpendicular to the film plane. A SQUID magnetometer was used to measure the temperature dependence of the magnetization. For this measurement, the sample was cooled to 10 K in the presence of a magnetic field of 2 T applied perpendicularly to the film. At 10 K, the magnetic field was removed, and the remanent magnetization was

measured as a function of temperature when the sample was heated. MOKE measurements were conducted in a polar configuration, in which the magnetic field was applied perpendicular to the film plane. The sweep time of the magnetic field for MOKE measurements was 60 mT/s. We investigated the stochastic behavior of the magnetic domain based on time-lapse magnetic-domain imaging using MOKE microscopy. Time-lapse MOKE microscopy is an established technique that is widely used for magnetic DW dynamics [4,8,24-27] owing to its short image acquisition time, the capability of various field/temperature sequences, and nondestructive techniques, in contrast to other techniques such as magnetic force microscopy and Lorentz microscopy. Figure 1 shows a schematic illustration of the MOKE microscope equipped with DC and pulsed magnets. This setup was equipped with a custom-developed pulse coil. A pulsed magnetic field was applied with the superimposition of the DC magnetic field H_{DC}. H_{DC} was applied using a permanent magnet, and the DC field strength $\mu_0 H_{DC}$ was varied by changing the distance d between the sample and permanent magnet. The permanent magnet for the DC field can be removed upon the zero-field cooling. The applied field was perpendicular to the film plane. Domain images were obtained using a CCD camera with an exposure time of 1/60 s. The observation temperature varied from 278 to 285 K. The film was cooled in zero magnetic field using a Peltier device, and the temperature was controlled with the accuracy of ±0.2 K using a PID circuit.

3. Results and Discussions

3.1 Structure of fabricated film

The RHEED images of each layer and the XRD profiles are shown in Figs. 2(a)–2(e). In the RHEED images of the Pt buffer and Cr_2O_3 layers (Figs. 2(a) and 2(b)), sharp streaks and a Laue zone were observed, thus indicating high crystalline quality and a flat surface. The diffraction pattern of the Cr_2O_3 surface was symmetric with respect to the 00 streak because twin domains with twin boundaries along $[11\bar{2}0]_{Cr2O3}$ were formed. Spots superimposed by the weak ring pattern were observed in the RHEED images of the Au, Co, and Pt capping layers. (Figs. 2(c)–2(e)) The spot pattern indicates the epitaxial growth of every layer, whereas the ring indicates that some layers were partially polycrystalline. In the XRD profile shown in Fig. 2(f), diffraction peaks assigned to Pt 111/Cr_2O_3 0006 and Pt 222/Cr_2O_3 00012 were observed. Diffractions from Pt(111) and Cr_2O_3(0006) could not be distinguished easily because their lattice spacings were extremely

similar. Laue oscillations were observed around the Pt 111/Cr_2O_3 0006 diffraction peaks (inset of Fig. 2(f)). The coherence length estimated from the oscillation period corresponded to the thickness of the Pt buffer layer.

3.2 Time evolution of magnetic domain pattern

Figure 3(a) shows the magnetization curve measured using the VSM at room temperature (~298 K). Rectangular and S-shaped loops were observed in directions perpendicular and parallel to the film plane, respectively, thus indicating that the film exhibited PMA. The effective uniaxial magnetic anisotropy energy density K_{eff} was 2.3×10^5 J/m^3, which is lower than the typical value for a Co/Pt multilayer [28] owing of the abovementioned partially polycrystalline nature. The inset of Fig. 3(a) shows the temperature dependence of the remnant magnetization. Although the Co layer was extremely thin (i.e., 0.6 nm), the Curie temperature was sufficiently higher than 300 K. Additionally, the film indicated a PEB below 284 K. A typical exchange-biased MOKE loop after field cooling is shown in Fig. 3(b). The MOKE loop showed a gentle slope around the coercivity, thus indicating the presence of a coercivity distribution. The coercivity distribution was regarded as the error of $\mu_0 H_C$. The definition of the average value $\mu_0 H_C$ and width $\Delta\mu_0 H_C$ are shown in in Fig. 3(b). The loop shifted in the positive direction owing to the negative cooling field. The exchange bias field, $\mu_0 H_{EX}$, exceeded the coercivity and $\mu_0 H_C$. Meanwhile, $\mu_0 H_{EX}$ and $\mu_0 H_C$ were deduced as $(\mu_0 H_{C1} + \mu_0 H_{C2})/2$ and $(\mu_0 H_{C1} - \mu_0 H_{C2})/2$, respectively. The definitions of $\mu_0 H_{C1}$ and $\mu_0 H_{C2}$ are presented in Fig. 3(b).

Figure 3(c) shows plots of $\mu_0 H_{C1}$ and $\mu_0 H_{C2}$ as functions of temperature. As shown, $\mu_0 H_{C1}$ decreased monotonically with increasing temperature; meanwhile. $\mu_0 H_{C2}$ showed a similar temperature dependence up to 280 K and began to exhibit an anomaly at 281 K. $\mu_0 H_{C2}$ increased rapidly at approximately 281.5 K and stabilized above 284 K. Figure 3(d) shows the temperature dependences of $\mu_0 H_{EX}$ and $\mu_0 H_C$, as defined above. $\mu_0 H_{EX}$ decreased gradually as the temperature increased up to 281 K, whereas $\mu_0 H_C$ remained almost stable in this temperature regime. $\mu_0 H_{EX}$ decreased rapidly at approximately 281. 5 K, which is associated with the peak of $\mu_0 H_C$, as observed in various exchange-biased systems [29-31].

By employing the ZFC to maintain the demagnetized state, the MOKE loop indicated a double-shifted loop, i.e., a dual PEB [16,21]. To form the dual-exchange-biased state, the sample was demagnetized using a decayed magnetic field

cycle at room temperature. Figure 4(a) shows a typical MOKE loop that exhibits a dual PEB. This finding agrees well with results of previous studies pertaining to films with similar stacking structures [16, 32]. The exchange-bias polarity was determined for each magnetic domain based on our previous study [32]. A time-lapse magnetic domain pattern was observed in the sole magnetic domain, which indicates a PEB. The time-dependent magnetic-field sequence is shown in Fig. 4(b). A pulsed magnetic field combined with a finite DC magnetic field was applied. The typical pulse shape is shown in Fig. 4(c). The pulse amplitude $\mu_0 H_{pls}$ exceeded 48 mT. The pulse width was set to 1/60 s, which is same as the exposure time of the CCD camera of the MOKE microscope. The field path along the dual-exchange-biased loop is shown in Fig. 4(a). Figure 4(d) shows the corresponding energy diagram at each point in the perpendicular exchange-biased regime. In the following section, we focus on the magnetization state in the perpendicular exchange-biased regime. Beginning from State A, where the magnetization decreased, a positive pulsed field was applied. The combination of $\mu_0 H_{pls}$ and $\mu_0 H_{DC}$ was sufficiently high to saturate the magnetization (State B). After removing the pulse field, only $\mu_0 H_{DC}$ remained, and the magnetic state changed to State C. Because this state was metastable, the magnetization was relaxed by thermal activation (dotted green line in Figs. 4(a) and 4(d)). To enable this scenario, $\mu_0 H_{DC}$ was set between $\mu_0 H_{EX}$ and $\mu_0 H_{C2}$. The value of $\mu_0 H_{DC}$ was varied from 6.0 and 19 mT depending on the measured temperature. The employed $\mu_0 H_{DC}$ condition at each temperature are indicated by the black bars in Fig. 2(c). The magnetic domain pattern was recorded during the field sequence with an acquisition time interval of 1/60 s, and $t = 0$ was defined as the time at which the pulse field was removed (Fig. 4(b)). Observations under the same DC field conditions were repeated typically 100 times. The magnetization of the negative-exchange-biased regime remained energetically stable along the field path above. Therefore, they were neither included in our investigation nor considered in the analysis.

Figure 5 shows the example of snapshots of the time-lapse magnetic domain observations. A triangular magnetic domain (dark gray region) was observed before a field was applied (State A in Fig. 4(a)). The angle θ in the triangular domain shown in Fig. 5(a) was ~60°, thus indicating that the edge direction of the triangle matched the crystallographic orientation of the film. In our case, the edge direction was parallel to $[11\bar{2}0]$ of the $Cr_2O_3(0001)$ layer, which should be along the twin boundary. When a pulsed field was applied, the magnetic domain vanished due to saturation (Fig. 5(b)) (see State B in Fig. 4(a)). Immediately after the pulsed field was removed (State C in Fig. 4(a)), the saturated state was

maintained because $\mu_0 H_{DC}$ was below the inherent switching field. At this point, the magnetization state was metastable, as shown in the energy diagram of State C (Fig. 4(d)). The metastable magnetization relaxed within a finite relaxation time τ. The relaxation manifested as the latency of the reversed magnetic domain nucleation. After a finite latency time t_L, the reversed magnetic domain nucleated at the top corner of the triangle (Fig. 5(c)). The t_L value was not constant because of the stochastic process, as shown in the supplementary movies. Nucleation occurred at the site (see the supplementary movies) where the exchange stiffness and/or effective magnetic anisotropy energy decreased, which is associated with the local frustration of the spin structure, the distribution of the demagnetizing field, and structural defects. In more than 90% of the trials, nucleation occurred in the same corner. Nucleation was not observed in the interior of the triangle. The nucleated magnetic domain expanded, thus indicating DW propagation (Figs. 5(d) and 5(e)). The DW preferentially propagated along the $[1\bar{1}00]$ direction of the $Cr_2O_3(0001)$ layer, as indicated by the blue arrow in Fig. 5(e). The DW propagated intermittently, thus suggesting creep motion. The DW edge shape in the propagation direction was rough, which is consistent with the creep motion of the DW [33]. Finally, the initial magnetic state, i.e., the triangular magnetic domain, recovered (Fig. 5(f)). The finite t_L and creep motion of the DW explicitly indicated that thermal activation significantly affected the recovery of the initial domain pattern. We confirmed that the same recovery process occurred in every $\mu_0 H_{DC}$. We could not capture the latency of the reversed domain nucleation above 282 K because t_L became shorter than the acquisition time. Therefore, we were able to evaluate only the DW propagation above 282 K. During the observations, no change was observed outside the triangle, e.g., the negative exchange-biased area, as mentioned above.

3.3 Stochastics of reversed domain nucleation

Figures 6(a)–6(c) show the examples of the t_L distribution obtained at 278 K via typically 100 attempts for each $\mu_0 H_{DC}$. At $\mu_0 H_{DC}$ = 16.7 mT, the distribution was sharp and t_L indicated a maximum value at approximately 0.03 s. As $\mu_0 H_{DC}$ increased, the distribution broadened and the t_L for the maximum probability increased, i.e.,: ~0.3 s for $\mu_0 H_{DC}$ = 17.6 mT (Fig. 6(b)) and ~3 s for $\mu_0 H_{DC}$ = 19.0 mT (Fig. 6(c)). Figure 6(d) shows the time required for the cumulative number of nucleation events to occur. The increase in $\mu_0 H_{DC}$, with the DC field being distant from the switching field (see Fig. 4(a)), resulted in a decrease in the driving force for magnetization reversal and consequently increased the time to the occurrence

of an event. Independent of the cumulative number of events, e.g., 15 and 50, the time for an event to occur exponentially increased with $\mu_0 H_{DC}$. If the nucleation event is a stochastic phenomenon, then the nucleation event is a memoryless property; in this case, the Poisson process governs the event. In the Poisson process, the event interval obeys the exponential distribution. The exponential increase in the time-to-event allows us to assume the Poisson process to describe the stochastics of the nucleation event. Considering a Poisson process with rate λ, the probability of the first Poisson event to occur until time t can be expressed using a gamma distribution with a probability density function [12].

$$P = \lambda t \exp(-\lambda t) \tag{1}$$

Equation (1) reproduces the t_L distribution well, as indicated by the solid lines in Figs. 6(a)–6(c). The t_L distribution provides the relaxation time of the magnetization τ as $1/\lambda$. The Poisson process follows the Arrhenius law for $1/\lambda$ [34].

$$\tau = \frac{1}{\lambda} = \tau_0 \exp\left(\frac{\Delta E}{k_B T}\right), \tag{2}$$

where τ_0 is the attempted reversal time, k_B the Boltzmann constant (1.38×10^{-23} J/K), and T the absolute temperature. ΔE is the energy barrier for the magnetization reversal, and τ_0 is fixed at 1 ns as a typical value. The τ values were obtained using the λ values obtained by fitting the histogram of t_L for each measurement condition. Figure 7 shows the change in τ with $\mu_0 H_{DC}$, i.e., τ increased monotonically with $\mu_0 H_{DC}$. The τ–$\mu_0 H_{DC}$ relationship is relevant to the changes in ΔE as a function of $\mu_0 H_{DC}$, which has been a long-standing issue. In the following section, we discuss ΔE and the relevant parameters.

The free energy when the reversed domain is nucleated is expressed as [11]

$$E = Lt\gamma - St\mu_0 H M_S, \tag{3}$$

where L and S are the DW length and the area of the nucleated domain, respectively; t is the thickness; M_S is the saturation magnetization; and γ is the DW energy density. By denoting r as the length relevant to the nucleated domain size, L and S are proportional to r and r^2, respectively. Because the valid expression of ΔE is nontrivial, we discuss two types of expressions for ΔE. When ΔE is regarded as the energy barrier for nucleation of the reversed domain, the following expression is widely used [35-38]:

$$\Delta E = E(r) - E(0) = E_0 \left(1 - \frac{\mu_0 H}{\mu_0 H_0}\right)^n \tag{4}$$

E_0 is the barrier height required to nucleate the reversed domain; H_0 is the intrinsic magnetization reversal field without

thermal agitation; and n is an exponent whose value ranges from 1 to 2 depending on the magnetization reversal process, and $n = 2$ was derived for the coherent rotation. Vreis *et al* discussed the nucleation conditions for a diamond-shaped island [15]. They showed that n might be 1 when the nucleated domain size is much smaller than the island size to be reversed, and when the DW pinning energy is weak such that the DW does not bend under the application of an external field. Furthermore, they expected a nonlinear ΔE–H relationship at extremely high energy barriers above 400 k_BT. Because magnetization relaxation cannot occur within an experimentally accessible timescale for such a high ΔE, we can reasonably assume $n = 1$. In this analysis, H in Eq. (3) was replaced by $H–H_{EX}$ to consider exchange bias, where H_{EX} denotes the exchange bias field without thermal agitation, and the $\mu_0 H_{EX}$ value used in the analysis differs from the value shown in Fig. 3(c). To avoid the discrepancy, we evaluated the H_{EX}-independent parameters, i.e., $E_0/\mu_0 H_0$ and $\mu_0 H_{EX} - \mu_0 H_0$. Figures 8(a) and 8(b) show the temperature dependences of $E_0/\mu_0 H_0$ and $\mu_0 H_{EX} - \mu_0 H_0$, respectively. The nucleation volume V_n can be extrapolated using ΔE [39]:

$$V_n = -\frac{\partial \Delta E}{\partial \mu_0 H} / M_S \tag{5}$$

M_S is the saturation magnetization [A/m] of the embryo. Using eq. (4) with $n = 1$, V_n can be expressed as

$$V_n = \frac{E_0}{\mu_0 H_0} / M_S \tag{6}$$

Thus, $E_0/\mu_0 H_0$ ($= V_n M_S$) [J/T] denotes the number of magnetic moments in the embryo. In the case of the simple FM layer, M_S can be determined by the material parameter, e.g. 1410 kA/m for pure Co. However, in our case, the precise determination of the M_S value is nontrivial due to the spin-polarization of adjacent heavy metal layers, Pt and Au, and the uncompensated AFM moments coupled with the FM moments. Based on the hypothesis that the reverse magnetic moment fully relies on Co, the embryo size is calculated as 70–100 nm in diameter, which is one order of magnitude higher than that reported for Co/Pt nanodots [28]. Because the embryo size should be comparable to the DW width [28], the anticipated large embryo size is attributable to the low K_{eff} of our film, which would increase the DW width. $\mu_0 H_{EX} - \mu_0 H_0$ is relevant to the switching field in the descending branch of the magnetization curve, e.g., $\mu_0 H_{C2}$ without thermal agitation. As shown in Fig. 8(b), $\mu_0 H_{EX} - \mu_0 H_0$ and $\mu_0 H_{C2}$ showed similar temperature dependences, although $\mu_0 H_{C2}$ was higher than $\mu_0 H_{EX} - \mu_0 H_0$ because of thermal agitation.

To compare the ΔE with those of other systems [15,40,41], we evaluated E_0 and H_0 by assuming the $\mu_0 H_{EX}$ value from the MOKE loop. As mentioned above, the apparent $\mu_0 H_{EX}$ value measured using MOKE magnetometry differed from the inherent $\mu_0 H_{EX}$ value. The uncertainty of the $\mu_0 H_{EX}$ value was regarded as the error of $\mu_0 H_{EX}$ (see Fig. 3(d)). The insets of Fig. 8(a) show the plot of E_0 as a function of temperature. E_0 was 1.4±0.6 eV at 278 K and decreased monotonically to approximately 0.8±0.3 eV at 281 K. Because the Curie temperature of the FM layer (Pt/Co/Au layer) was sufficiently higher than the measurement temperature regime, as confirmed from the *M–T* curve (inset of Fig. 3(a)), the temperature-dependent E_0 suggests that the magnetic anisotropy energy density of the AFM layer significantly affects E_0.

The temperature dependence of $\mu_0 H_0$ is shown in the inset of Fig. 8(b). The $\mu_0 H_C$ value was higher than $\mu_0 H_C$ (= $(\mu_0 H_{C1} - \mu_0 H_{C2})/2$ (see Fig. 3(d)), as determined via MOKE measurements. $\mu_0 H_0$ increased with temperature, as was the case for $\mu_0 H_C$. Because the enhancement in $\mu_0 H_C$ near T_N can be attributed to the fluctuating spin structure in the AFM layer [29-31,42], the similar temperature dependences $\mu_0 H_0$ and $\mu_0 H_C$ suggest that the AFM spin fluctuation inherently enhances the switching field.

Next, we compare the deduced E_0 and $\mu_0 H_0$ values with those of other systems. Table I summarizes the E_0, $\mu_0 H_0$ and K_{eff} values for some systems. The E_0 value for our evaluation was lower than that of Co(0.9 nm)/Pt(2 nm) multilayer nanodots [40] and similar to that of Co(0.3 nm)/Pt(0.3 nm) multilayer nanodots [15]. The E_0 values appeared to correlate with K_{eff}. This is reasonable because E_0 is hypothetically proportional to $K_{eff} \cdot V$ (V: volume of the embryo), as originally derived from the Stoner–Wohlfarth model [35]. A positive correlation between E_0 and K_{eff} has been reported for Co/Pt multilayer nanodots [28], which is consistent with the prediction above. The $Co_{80}Pt_{20}$ nanodots showed high E_0 and $\mu_0 H_0$ values despite the moderate K_{eff} [41]. This is attributed to the difference in the switching modes. The switching mode for the Co/Pt multilayer nanodots was the nucleation of the embryo and rapid growth [40], whereas the $Co_{80}Pt_{20}$ nanodots showed coherent rotation [41]. A similar trend was observed for $\mu_0 H_0$, which is consistent with the positive correlation between E_0 and $\mu_0 H_0$ [6].

An alternative expression for ΔE can be derived from the droplet model [11,43,44], i.e.,

$$\Delta E = E(r_0) - E(r) = \eta \left(\frac{1}{\mu_0 H} - \frac{1}{\mu_0 H_0} \right), \quad (7)$$

where η denotes a constant related to the DW depinning force; r_0 is the droplet radius at which γ shows the highest gradient with respect to r; where $\partial\gamma/\partial r$ is maximum at r_0; and H_0 is the highest depinning field of the DW propagation. Based on the hypothesis of using the mean $\mu_0 H_{EX}$ shown in Fig. 2(c), $\mu_0 H_0$ falls into the negative $\mu_0 H_0$ value (not shown), thus indicating that the energy barrier does not decrease to zero, which is unrealistic. This discrepancy is owing to the difference in the reversal mechanism of the droplet model. Equation (7) was derived based on the DW propagation after nucleation, and H_0 denotes the deepening field of the DW propagation. The τ value used in the analysis is the latency time, e.g., the nucleation event of the embryo.

3.4 Creep motion of DW

We further investigated the effect of the AFM layer on the switching behavior based on the DW velocity v. As mentioned above, the MOKE observations suggest the creep motion of the DW. Based on the time evolution of the magnetic domain pattern, we analyzed v for each $\mu_0 H_{DC}$. Figure 9(a) shows the change in v with $\mu_0 H_{DC}$, where v is typically less than 1.5 mm/s. For each measurement temperature, v decreased as $\mu_0 H_{DC}$ decreased i.e., being apart from $\mu_0 H_0$ (or $\mu_0 H_{C2}$). v–$\mu_0 H_{DC}$ was monotonic, except at 283 K, and appeared to be nonlinear. As the temperature increased, the change in v becomes gentle. At 283 K, which is approximately T_B, v indicated a large dispersion. We analyzed the v–$\mu_0 H_{DC}$ relationship based on the creep motion of the DW. In the creep regime, v is proportional to $H^{1/4}$ [33,45]. Combining this with the exchange bias field, the v for the exchange-biased film can be expressed as

$$v = v_0 \exp\left[-\frac{U_C}{k_B T}\left(\frac{\mu_0 H_{crit}}{\mu_0 H - \mu_0 H_{EX}}\right)^{1/4}\right] \quad (8)$$

Here, v_0 is the perfector, U_C the pinning potential, and H_{crit} the switching field. Figure 9(b) shows a plot of v as a function of $(\mu_0 H_{DC} - \mu_0 H_{EX})^{-1/4}$. For the analysis, we assumed experimentally obtained $\mu_0 H_{EX}$ (Fig. 3(c)) values. Except at 283 K, the plots exhibited a linear relationship, thus supporting the DW motion expressed in Eq. (8). At 283 K, v was highly dispersed, and the linear relationship disappeared. As shown in Fig. 3(c), 283 K is approximately T_B and the coercivity shows a significant enhancement. As discussed previously, the AFM spin structure fluctuated significantly at this temperature. The fluctuating AFM spin structure may be highly disturbed by the external magnetic field, as manifested by the divergence of

magnetic susceptibility at T_N [46], which would yield a nonuniform U_C.

Figure 10 shows the temperature dependence of $U_C(\mu_0 H_{crit})^{1/4}$. Below 281 K, $U_C(\mu_0 H_{crit})^{1/4}$ was 0.50–0.63 eV $T^{1/4}$ and temperature independent. Above 283 K, $U_C(\mu_0 H_{crit})^{1/4}$ decreased to 0.063–0.31 eV·$T^{1/4}$. Based on the hypothesis that $\mu_0 H_{crit}$ corresponds to $\mu_0 H_{C2}$, U_C in a temperature unit was deduced as 20000–25000 K below 281 K and 2000–8000 K above 283 K. Compared with the temperature dependence of $\mu_0 H_{EX}$ shown in Fig. 3(d), the U_C value increased at T_B, whereas it was temperature independent in each temperature regime, e.g., below and above T_B. In the case of FM layers without an AFM layer, such as Pt/Co/Pt [47,48] and Au/Co/Au [49] films, U_C was almost independent of temperature. Hence, the increase in $U_C(\mu_0 H_{crit})^{1/4}$ indicates that AFM ordering enhances the depinning potential of DW propagation.

4. Summary

We investigated the stochastics of reversed magnetic domain nucleation using individual magnetic domains to eliminate the energy barrier distribution, which is difficult in magnetization measurements for large magnetic entities. In particular, we exploited the robust magnetic domain structure in a dual perpendicular exchange-biased system, i.e., the Pt/Co/Au/Cr_2O_3/Pt film. Time-lapse magnetic domain observations captured the recovery process of the magnetic domain pattern after a pulsed magnetic field was applied. The recovery process included the nucleation of the reversed domain and subsequent DW creep. The reversed domain nucleated after a finite latency, which indicated that nucleation involved a stochastic event with thermal activation. Multiple trials revealed that the Poisson process accurately described the nucleation stochastics. The relaxation time for the nucleation event τ increased with the constant DC magnetic field. The DC-field dependence of τ was analyzed using two types of energy-barrier functions. The estimated parameters, E_0 and η, which are both relevant to the DW energy, decreased monotonically as temperature increased. The intrinsic magnetization reversal field H_0 evaluated from the nucleation model showed a similar temperature dependence of the coercivity, which suggested the significant contribution of the AFM spin fluctuation near T_B. However, H_0 became negative near T_B, thus suggesting that the droplet model was inappropriate for describing the switching event.

The DW propagation was dominated by the creep mechanism. The analysis of DW creep revealed that the pinning potentials of DW and U_C increased at T_B. Below and above T_B, U_C was almost independent of temperature. Near T_B, the

magnetic field dependence of the DW velocity was highly dispersed, which was related to the AFM spin fluctuation. Hence, AFM ordering significantly affected the pinning potential of DW creep and the nucleation of the reversed domain. This study provides comprehensive understanding into the coercivity mechanism and magnetization reversal in perpendicular exchange-biased systems and contributes to the thermal stability of magnetic/spintronic devices.

Supplementary movies

Movie created using time-lapse images of magnetic domain evolution. The observation conditions were as follows: $\mu_0 H_{DC}$ = 19.0 mT and T = 278 K.

Acknowledgements

This study was partially supported by JSPS KAKENHI (project nos. 22H01757 and 22K18903) and the Iketani Science and Technology Foundation (project no. 0341023-A).

Data availability

Data supporting the findings of this study are available from the corresponding author upon reasonable request.

Declaration of Competing Interest

The authors declare that they have no competing financial interests or personal relationships that may have influenced the work reported herein.

Figure captions

Figure 1 Schematic illustration of MOKE microscope setup with sample cooling system using Peltier device, pulse coil, and permanent magnet for $\mu_0 H_{DC}$. Strength of $\mu_0 H_{DC}$ was varied by changing the distance d between the sample and permanent magnet surface.

Figure 2 RHEED images for (a) Pt buffer layer, (b) Cr_2O_3, (c) Au, (d) Co, and (e) Pt capping layer. Electron azimuth is $[11\bar{2}0]$ of α-Al_2O_3(0001) substrate. (f) $2\theta/\omega$ XRD profile. * represents diffraction peaks from substrate. Inset shows enlarged image around $2\theta/\omega = 40°$

Figure 3 (a) Magnetization curves measured at room temperature (~296 K). Red and black curves represent curve for applied field direction perpendicular and parallel to film plane, respectively. Inset of (a) shows temperature dependence of remanent magnetization. (b) Typical MOKE loop exhibiting exchange bias after field cooling. Curve shown in (b) was measured at 278 K after field cooling. In (b), the definition and anticipated range of $\mu_0 H_{C1}$ and $\mu_0 H_{C2}$ are shown. (c) Temperature dependence of $\mu_0 H_{C1}$ (open square, orange) and $\mu_0 H_{C2}$ (open circle, green). Black bars represent $\mu_0 H_{DC}$ range applied in time-lapse domain observation (see Fig. 1). (d) Temperature dependence of $\mu_0 H_{EX}$ (red circle) and $\mu_0 H_C$ (blue circle).

Figure 4 (a) Typical MOKE loop exhibiting dual exchange bias after zero-field cooling measured at 278 K. In (a), the field sequence for time-lapse domain observations and the corresponding magnetic states are shown. (b) Time sequence of applied magnetic field. Pulse magnetic field was applied superimposed with DC field. (c) Typical pulse field shape as a function of time. Pulse height exceeded 48 mT and is typically 50 mT. (d) Energy diagram at magnetic states A, B and C for magnetization in the positive exchange-biased region. Black dots and thick blue arrows represent hypothetical magnetization direction at each state. In metastable state C, the magnetization can relax within the relaxation time τ via thermal activation (broken green arrow).

Figure 5 Images of magnetic domain pattern: (a) Initial state, i.e., before applying pulse; (b) saturated state immediately after applying $\mu_0 H_{pls}$, (c) Nucleated state after finite latency, (d), (e) DW propagation and (f) final state, which is a perfectly recovered state and exhibits the same pattern as shown in (a). In (a) and (e), the crystallographic orientations of Cr_2O_3 layer are shown. Images shown are based on T = 278 K and $\mu_0 H_{DC}$ = 19.0 mT.

Figure 6 Example of t_L distribution obtained at $\mu_0 H_{DC}$ of (a) 16.7 mT, (b) 17.6 mT, and (c) 19.0 mT. All histograms shown were obtained at the observation temperature of 278 K. Red curves show results fitted using Eq. (1) with the amplitude factor. The time interval of histogram was adjusted for the easy comparison. (d) Changes in t_L at which the cumulative numbers of events are 15 and 50 for every measurement temperature. Lines represent results fitted using exponential function.

Figure 7 $\mu_0 H_{DC}$ dependence of τ. Black, red, blue, and green dots represent data measured at 278, 279, 280 and 281 K, respectively. Lines represent results fitted using Eq. (2).

Figure 8 Temperature dependence of (a) $E_0/\mu_0 H_0$ and (b) $\mu_0 H_{EX}$ - $\mu_0 H_0$. In (b), $\mu_0 H_{C2}$ deduced from Fig. 2(c) is plotted using open squares. Insets of (a) and (b) represent temperature dependence of E_0 and $\mu_0 H_0$, respectively, based on an assumed $\mu_0 H_{EX}$ value (see text).

Figure 9 (a) $\mu_0 H_{DC}$ dependence of DW velocity v for every measurement temperature. (b) v as a function of $[\mu_0 H_{DC} - \mu_0 H_{EX}]^{-1/4}$. Lines in (b) represent results fitted using Eq. (6).

Figure 10 Temperature dependence of $U_C(\mu_0 H_{crit})^{1/4}$. Dotted gray line provide visual guidance.

References

1. K. Miyazawa, S. Okamoto, T. Yomogita, N. Kikuchi, O. Kitakami, K. Toyoki, D. Billington, Y. Kotani, T. Nakamura, T. Sasaki, T. Okubo and K. Hono, Acta Materialia, 162, 1 (2019).
2. I. M. Miron, K. Garello, G. Gaudin, P-J. Zermatten, M. V. Costachem S. Auffret, S. Bandiera, B. Rodmaq, A. Schuhl and P. Gambardella, Nature, 476, 189 (2011).
3. D. Weller and A. Moser, IEEE Trans. Magn. 35, 4423 (1999).
4. F. Rodmaq, S. Pizzini, F. Yokaichiya, M. Bonfim, Y. Pennec, J. Camarero, J. Vogel, J. Sort, F. Garcia, B. Rodmaq, and B. Dieny, Phys. Rev. B 72, 134410 (2005).
5. S. Okamoto, R. Goto, N. Kikuchim O. Kitakami, T. Akiya, H. Sepehri-Amin, T. Ohkubo, K. Hono, K. Hioki, and A. Hattori, J. Appl. Phys. 118, 223903 (2015).
6. T. Yomogita, S. Okamoto, N. Kikuchi, O. Kitakami, H. Sepehri-Amin, Y. K. Takahashi, T. Ohkubo, K, Hono, K. Hioki and A. Hattori, Acta Materialia, 201, 7 (2020).
7. W. F. Brown Jr, Rev. Mod. Phys. 17, 15 (1945).
8. J. Ferŕe, V. Grolier, P. Meyer, S. Lemerle, A. Maziewski, E. Stefanowicz, S. V. Tarasenko, V. V. Terasenko, M. Kisielewski, and D. Renard, Phys. Rev. B 55, 15092 (1997).
9. W. Wernsdorfer, E. B. Orzco, K. Hasselbach, A. Benoit, B. Barbara, N. Demoncy, A. Loiseau, H. Pascard, and D. Mailly, Phys. Rev. Lett. 78, 1791 (1997).
10. R. D. Kirby, M. Yu and D. J. Sellmyer, J. Appl. Phys. 87, 5696 (2000).
11. J. Moriz, B. Dieny, J. P. Noziéres, Y. Pennec, J. Camarero, and S. Pizzini, Phys. Rev. B 71, 1000402(R) (2005).
12. E. Pineda and D. Crespo, Phys. Rev. E 78, 021110 (2008).
13. P. Bouquin, J-V. Kim, O. Bulynck, S. Rao, S. Couet, G. S. Kar, and T. Devolder, Phys. Rev. Appl. 15, 024037 (2021).
14. M-Y. Im, P. Fischer, D-H. Kim, K-D. Lee, S-H. Lee, S-C. Shin, Adv. Mater. 20, 1750 (2008).
15. J de. Vreis, T. Bolhuis and L. Abelmann, New J. Phys. 19, 093019 (2017).
16. Y. Shiratsuchi, S. Yoshida, H. Yoshida, Y. Kotani, K. Toyoki, R. Nakatani, C. Mitsumata and T. Nakamura, J. Appl. Phys. 127, 153902 (2020).
17. J. Jia, Y. Chen, B. Wag, B. Han, Y. Wu, Y. Wang, and J. Cao, J. Phys. D: Appl. Phys. 52, 065001 (2019).
18. Y. Shiratsuchi, W. Kuroda, T. V. A. Nguyen, Y. Kotani, K. Toyoki, T. Nakamura, M. Suzuki, K. Nakamura and R. Nakatani, J. Appl. Phys. 121, 073902 (2017).
19. K. D. Belashchenko, Phys. Rev. Lett. 105, 147204 (2010).

20. K. Toyoki, Y. Shiratsuchi, T. Nakamura, C. Mitsumata, S. Harimoto, Y. Takechi, T. Nishimura, H. Nomura and R. Nakatani, Appl. Phys. Express 7, 114201 (2014).
21. Y. Shiratsuchi and R. Nakatani, Mater. Trans. 57, 781 (2016).
22. X. He, Y. Wang, N. Wu, A. N. Caruso, E. Voscovo, K. D. Belashchenko, P. A. Dowben, and C. Binek, Nature Mater. 9, 579 (2010).
23. Y. Shiratsuchi, K. Toyoki, and R. Nakatani, J. Phys. Condens. Mater. 33, 243001 (2021).
24. J. Pommier, P. Meyer, G. Pénissard, J. Ferré, P. Bruno, D. Renard, Phys. Rev. Lett. 65 (1990) 2054–2057
25. M. Yamanouchi, J. Ieda, F. Matsukura, S. E. Barns, S. Maekawa and H. Ohno, Science 317, 1726 (2007).
26. U. Bauer, L. Yao, A. Jun Kan, P. Agrawal, S. Emori, H. L. Tuller, S. van Dijken, and G. S. D. Beach, Nature Mater. 14, 174 (2015).
27. W. Jiang, P. Upadhyaya, W> Zhang, G. Yu, M. Benjamin Jungfleisch, F. Y. Fradin, J. E. Peason, Y. Tserkovyak, K. L. Wang, J. Heinonen, S. G .E. te Velthuis, and A. Hoffmann, Science 349, 283 (2015).
28. S. Okamoto, T. Kato, N. Kukuchi, O. Kitakami, N. Tezuka and S. Sugimoto, J. Appl. Phys. 103, 07C501 (2008).
29. F. Funcomer and S. H. Charap, J. Appl. Phys. 43, 4190 (1972).
30. M. D. Stiles and R. D. McMecheal, Phys. Rev. B 60, 12950 (1999).
31. C. Leighton, M. R. Fitzsimmons, A. Hoffmann, J. Dura, C. F. Majkzak, M. S. Lund, and I. K. Schuller, Phys. Rev. B 65, 054403 (2002).
32. Y. Shiratsuchi, S. Watanabe, H. Yoshida, N. Kishida, R. Nakatani, Y. Kotani, K. Toyoki and T. Nakamura, Appl. Phys. Lett. 113, 242404 (2018).
33. S. Lemerle, J. Ferŕe, C. Chappert, V. Mathet, T. Giamarchi, and P. L. Doussal, Phys. Rev. Lett. 80, 849 (1998).
34. R. Ramesh and K. Srikrishna, J. Appl. Phys. 64, 6406 (1988).
35. E. C. Stoner and E. P. Wohlfarth, Philos. Trans. R. Soc. Lond., Ser. A 240, 599 (1948).
36. R. H. Victora, Phys. Rev. Lett. 63, 457 (1989).
37. W. Wernsdorfer, E. B. Orozco, K. Hasselbach, A. Benoit, B. Barbara, N. Demoncy, A. Loiseau, H. Pascard, and D. Mailly, Phys. Rev. Lett. 78, 1791 (1997).
38. P. Gaunt, J. Appl. Phys. 59, 4129 (1986).
39. D. Givord, A. Lienard, P. Ternaud, T. Viadieu, J. Magn. Magn. Mater. 67 L281 (1987).
40. N. Kikuchi, Y. Suyama, S. Okamoto and O. Kitakami, J. Appl. Phys. 109, 07B904 (2011).
41. K. Mitsuzuka, N. Kikuchi, T. Shimatsu, O. Kitakami, H. Aoi, H. Muraoka and J. C.

Lodder, IEEE Trans. Magn. 43, 2160 (2007).
42. C. Leighton, J. Nogués, B. J. Jönsson-Åkerman, and I. K. Schuller, Phys. Rev. Lett. 84, 3466 (2000).
43. B. Barbara and M. Uehara, IEEE Trans. Magn. 12, 997 (1976).
44. B. Barbara, J. Magnin, and H. Jouve, Appl. Phys. Lett 31, 133 (1977).
45. V. Jeudy, R. Diaz Pardo, W. Savero Torres, S. Bustingorry, and A. B. Kolton, Phys. Rev. B 98, 054406 (2018).
46. Y. Shiratsuchi, Y. Tao, R. Tsutsumi, K. Toyoki and R. Nakatani, J. Appl. Phys. 130, 193921 (2021).
47. R. Diaz Pardo, W. Savero Torres, A. B. Kolton, S. Bustingorry, and V. Jeudy, Phys. Rev. B 95, 184434 (2017).
48. J. Gorchon, S. Bustingorry, J. Ferŕe、V. Jeudy, A. B. Kolton, and T. Giamarchi, Phys. Rev. Lett. 113, 027205 (2014).
49. A. Kirilyuk, J. Ferŕe, V. Grolier, J. P. Jamet and D. Denard, J. Magn. Magn. Mater. 171, 45 (1997).

Table 1

Comparison of E_0, $\mu_0 H_0$, and $K_{\text{eff.}}$ For the case at room temperature (r.t.), T = 300 K was assumed to deduce E_0.

	E_0	$\mu_0 H_0$	K_{eff}	T	Ref.
Co(0.3)/Pt(0.3) nanodot	1.74 eV	67 mT	0.38 MJ/m^3	300 K	15
Co(0.9)/Pt(2) nanodot	5.6 eV	500 mT	2.0 MJ/m^3	r.t.	39
$Co_{80}Pt_{20}$(20) nanodot	17 – 21 eV	600 – 800 mT	1.2 MJ/m^3	r.t.	40
Pt(2)/Co(0.6)/Au(1.0) /Cr_2O_3(130)/Pt(20)	0.77 – 1.39 eV	28 – 35 mT	0.23 MJ/m^3 @r.t.	278 – 281 K	This work

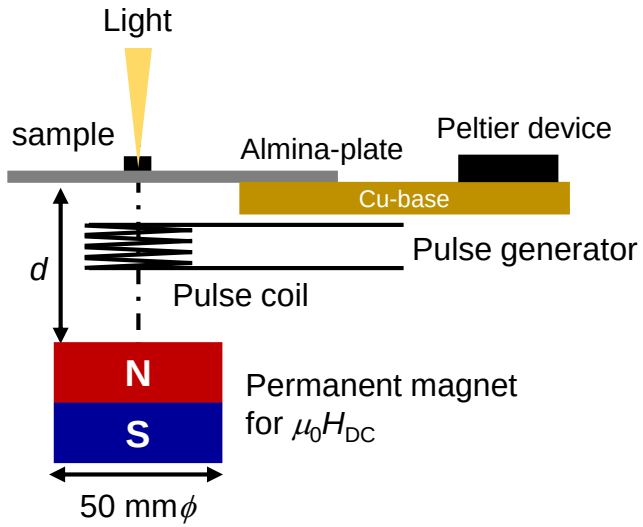

F. Luo *et al.*
Figure 1

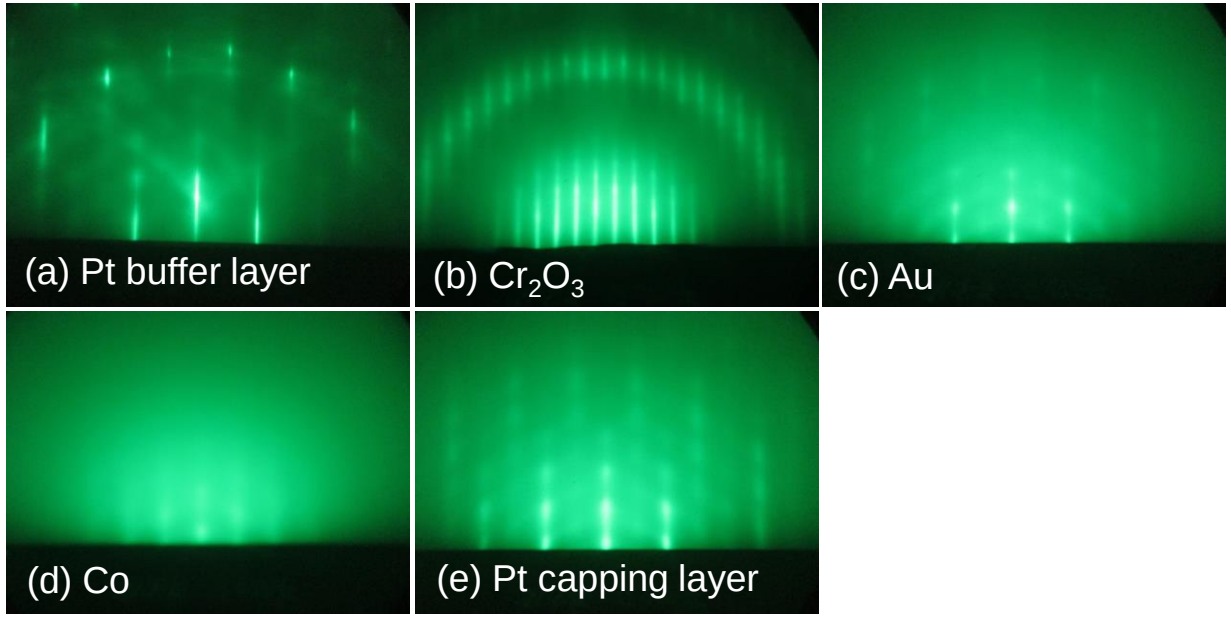

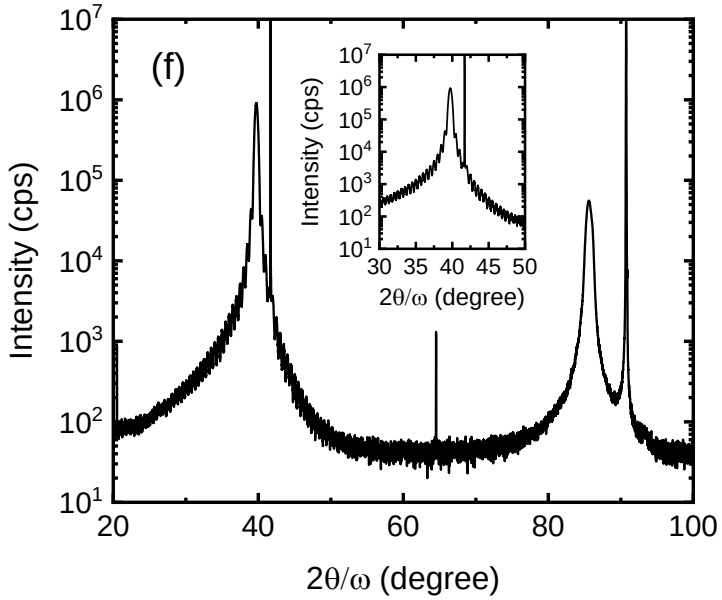

F. Luo *et al.*
Figure 2

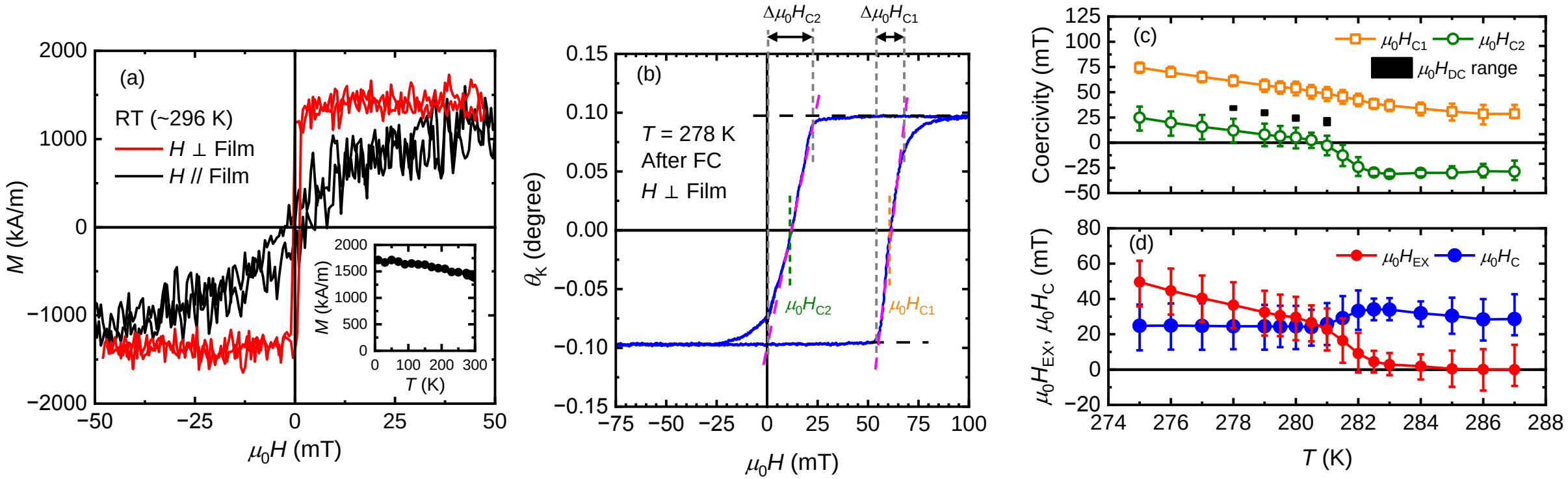

F. Luo *et al.*
Figure 3

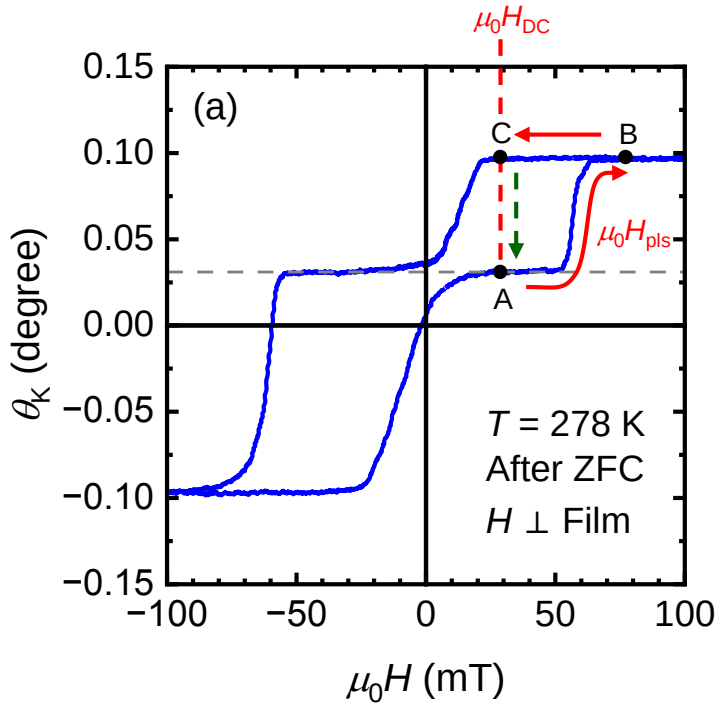

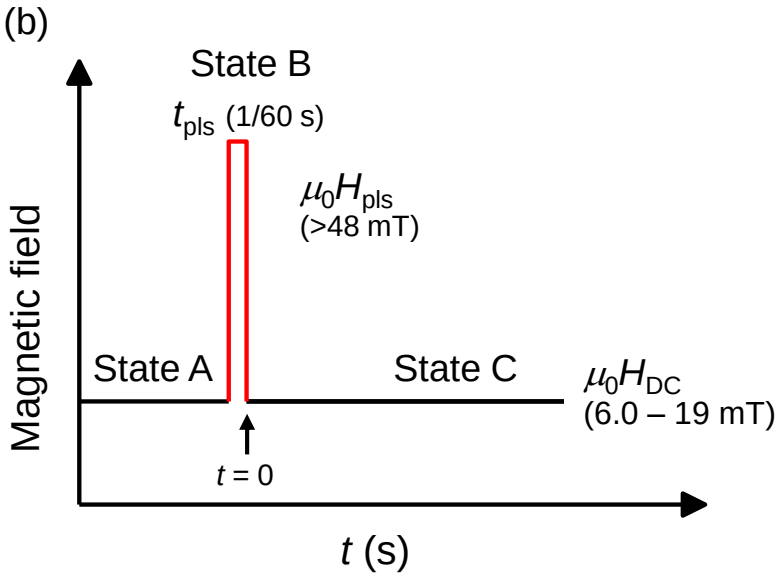

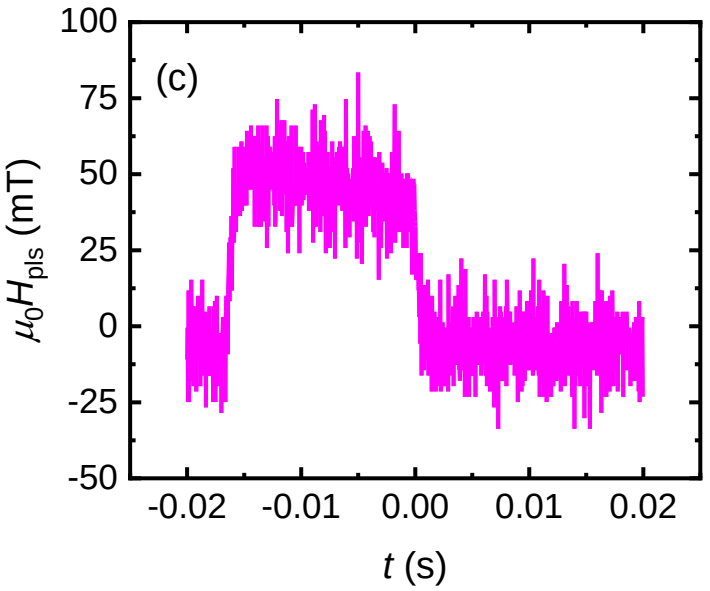

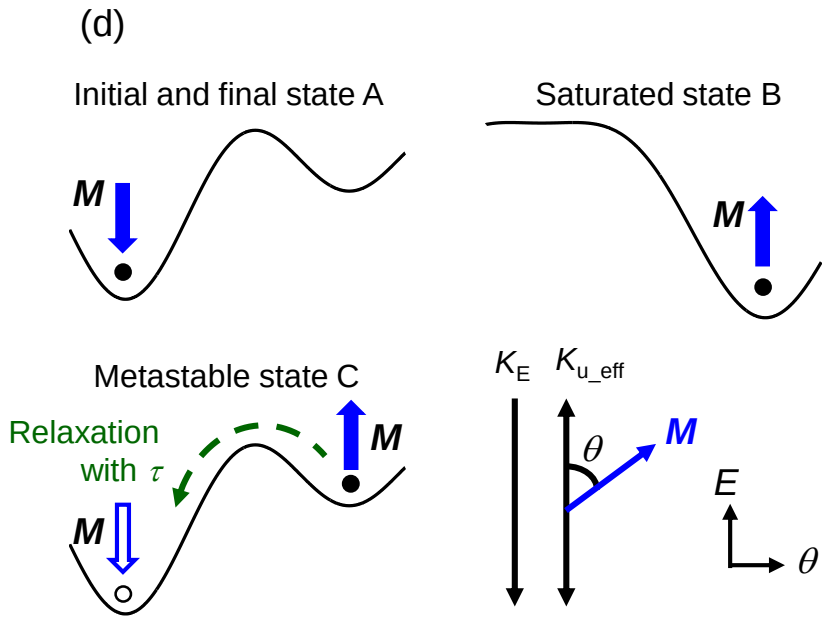

F. Luo *et al.*
Figure 4

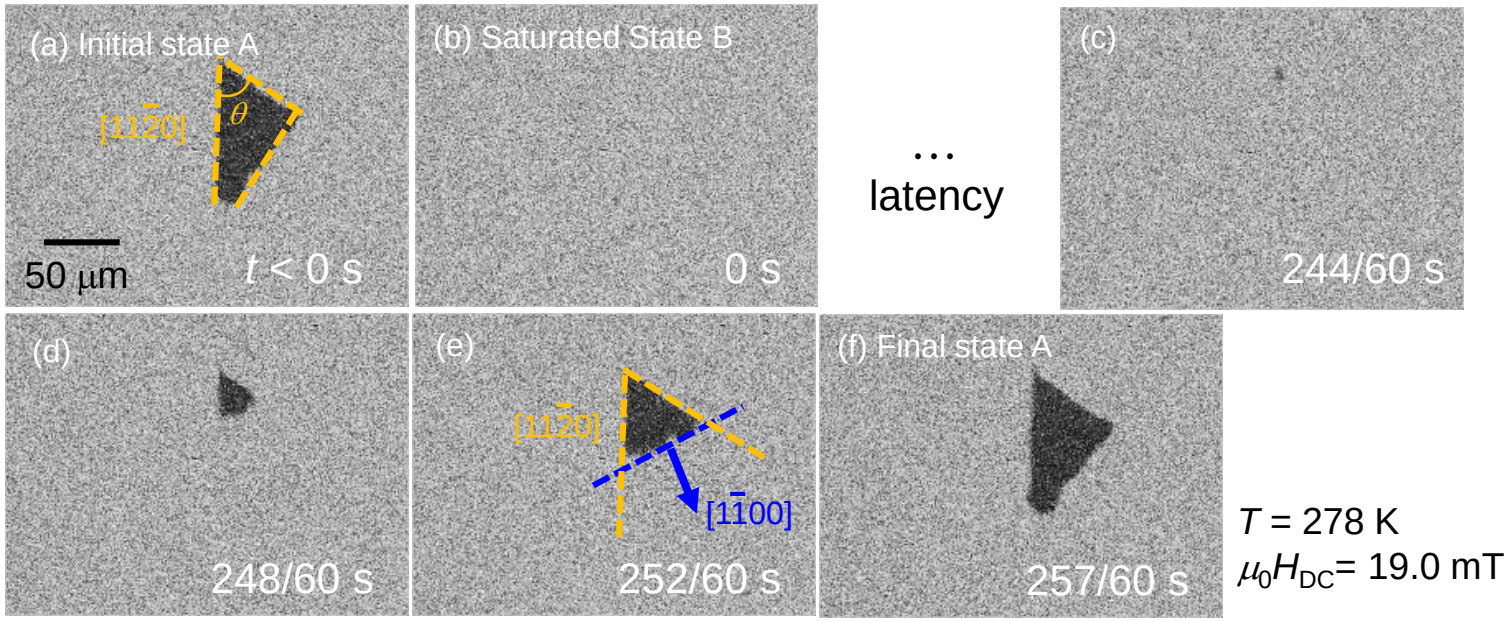

F. Luo *et al.*
Figure 5

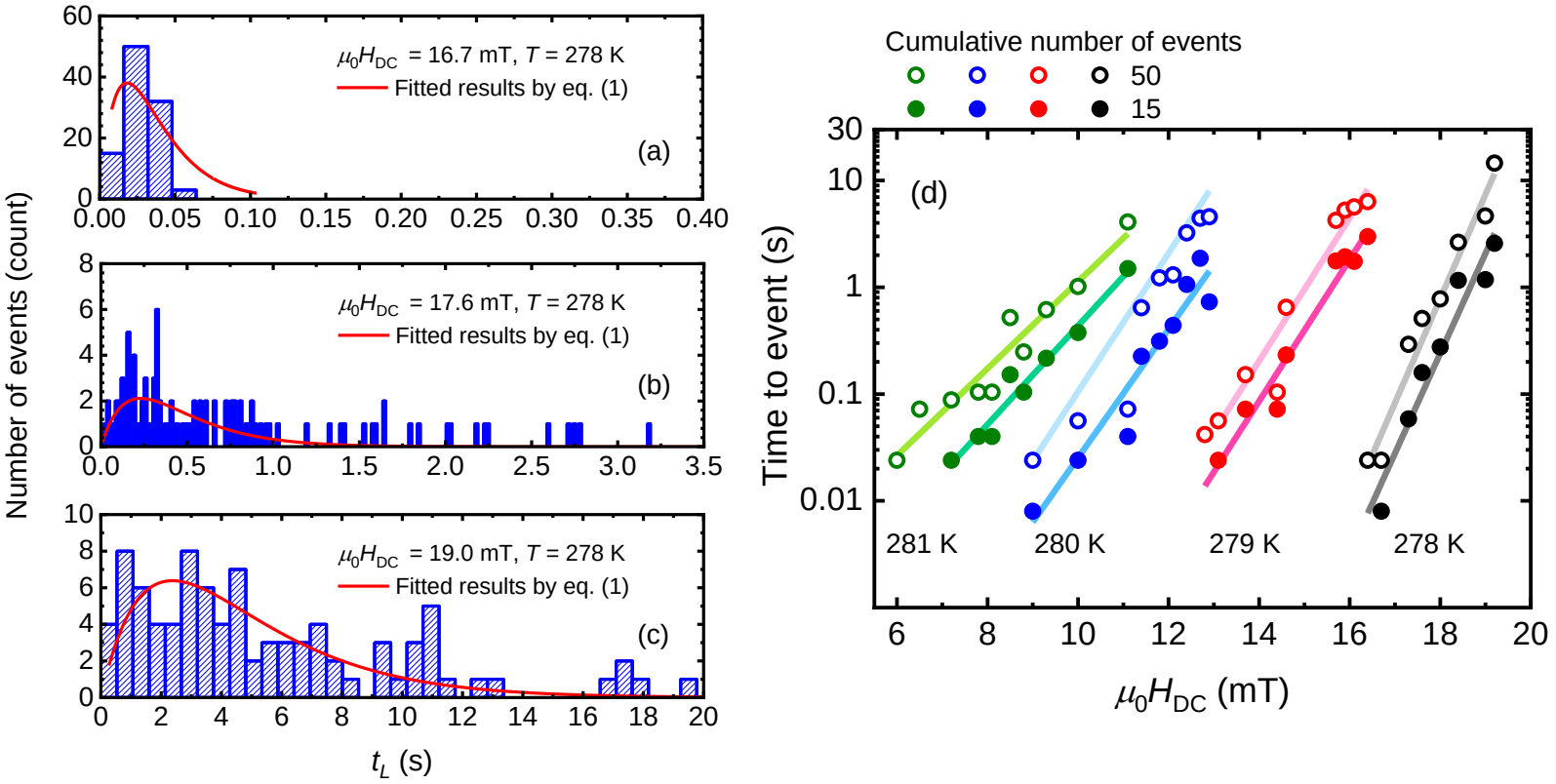

F. Luo *et al.*
Figure 6

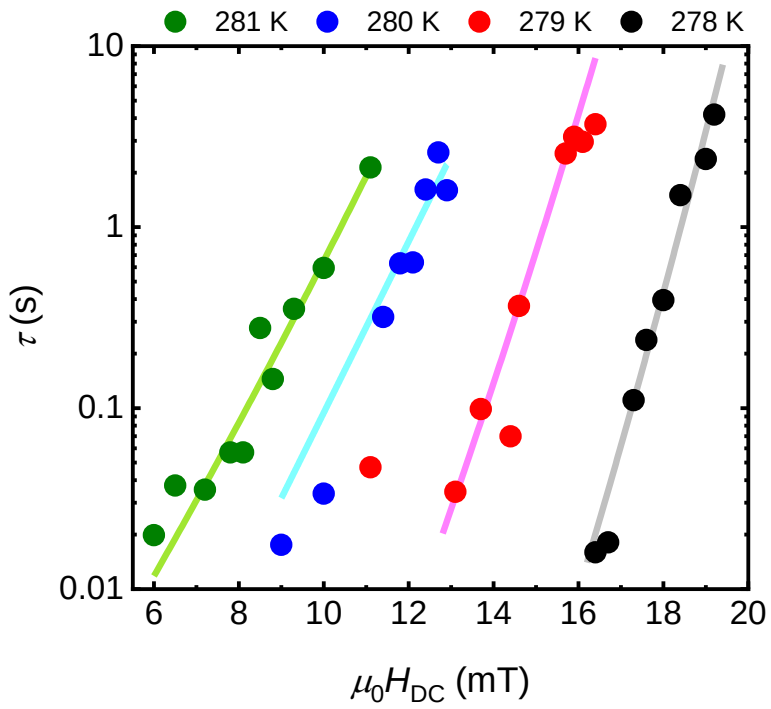

F. Luo *et al.*
Figure 7

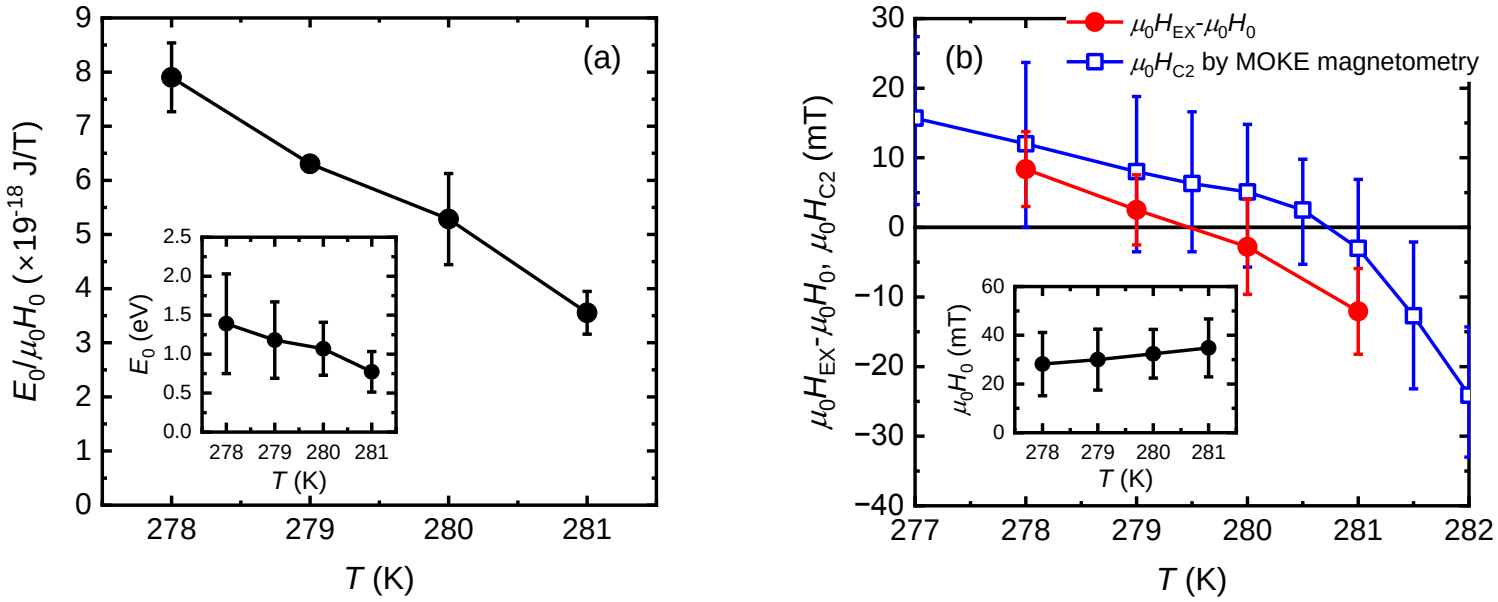

F. Luo *et al.*
Figure 8

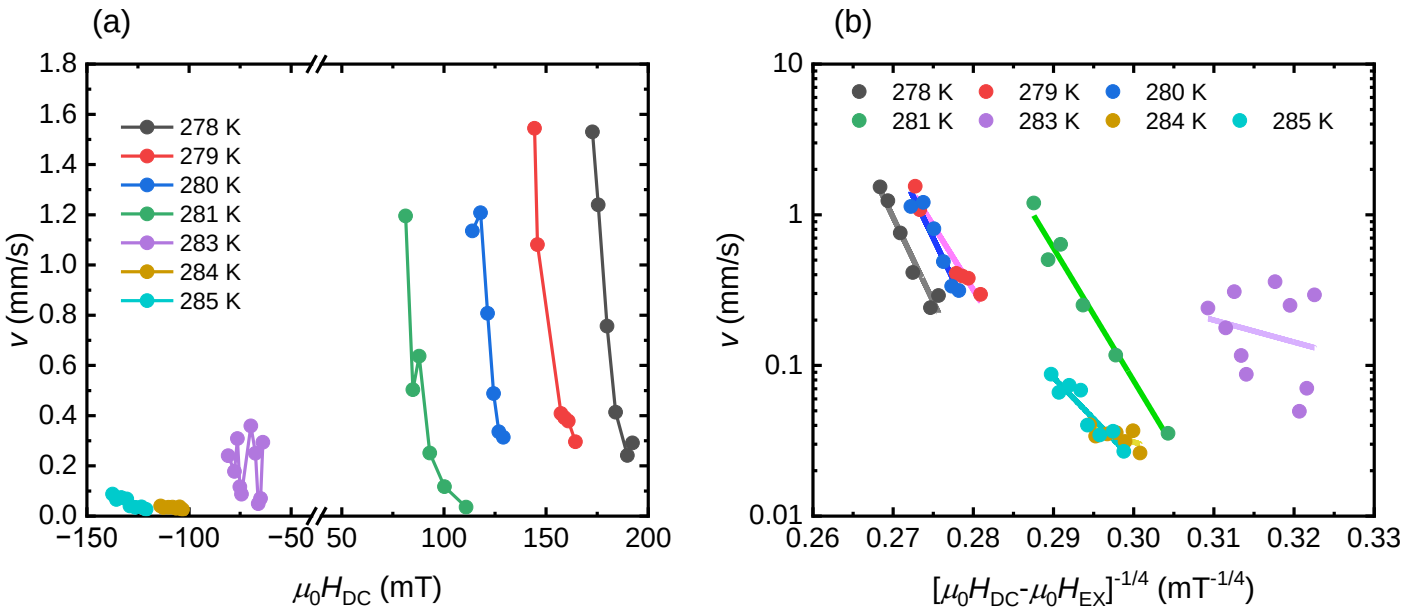

F. Luo *et al.*
Figure 9

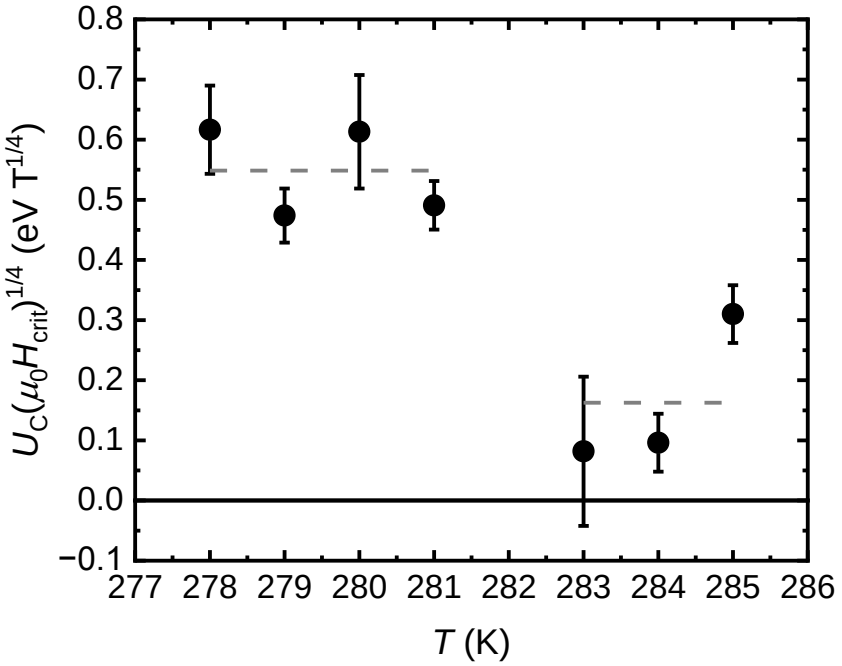

F. Luo *et al.*
Figure 10

Declaration of interests

☐The authors declare that they have no known competing financial interests or personal relationships that could have appeared to influence the work reported in this paper.

☒The authors declare the following financial interests/personal relationships which may be considered as potential competing interests:

Yu Shiratsuchi reports financial support was provided by Japan Society for the Promotion of Science. Yu Shiratsuchi reports financial support was provided by Iketani Science and Technology Foundation. Yu Shiratsuchi reports a relationship with Japan Society for the Promotion of Science that includes: funding grants.

Author statement

Fangfer Luo: Investigation
Kentaro Toyoki: Methodology, Formal analysis, Writing - Review & Editing
Chiharu Mitsumata: Formal analysis, Writing - Review & Editing
Jiaqi Shen: Investigation
Ryoichi Nakatani: Writing - Review & Editing
Yu Shiratsuchi: Conceptualization, Methodology, Formal analysis, Writing - Original Draft, Supervision